

Research Paper

OzDES Reverberation Mapping Program: CIV lags from six years of data

Andrew Penton¹, Hugh McDougall¹, Tamara M. Davis¹, Zhefu Yu², Umang Malik³, Paul Martini^{4,5}, Brad E. Tucker³, Christopher Lidman^{6,3}, Geraint F. Lewis⁷, Rob Sharp³, Michel Agüena^{8,9}, Sahar Allam¹⁰, Felipe Andrade-Oliveira¹¹, Jacobo Asorey¹², David Bacon¹³, Sebastian Bocquet¹⁴, David Brooks¹⁵, Ryan Camilleri¹, Aurelio Carnero Rosell^{16,9,17}, Daniela Carollo⁸, Anthony Carr¹⁸, Jorge Carretero¹⁹, Ting-Yun Cheng²⁰, Luiz da Costa⁹, Maria Elidaiana da Silva Pereira²¹, Juan De Vicente²², Shantanu Desai²³, Spencer Everett²⁴, Juan Garcia-Bellido²⁵, Karl Glazebrook²⁶, Daniel Gruen¹⁴, Gaston Gutierrez¹⁰, Samuel Hinton¹, Devon L. Hollowood²⁷, Klaus Honscheid^{4,28}, Kyler Kuehn²⁹, Ofer Lahav¹⁵, Sujeong Lee³⁰, Marisa March³¹, Jennifer Marshall³², Juan Mena-Fernández³³, Ramon Miquel^{34,19}, Justin Myles³⁵, Ricardo Ogando^{36,37}, Andrés A. Plazas Malagón^{2,38}, Anna Porredon^{22,39}, Martin Rodriguez Monroy^{25,40}, Kathy Romer⁴¹, Eusebio Sanchez²², David Sanchez Cid^{22,11}, Mathew Smith⁴², Marcelle Soares-Santos¹¹, Eric Suchyta⁴³, Molly Swanson⁴⁴, Vinu Vikram⁴⁵, Noah Weaverdyck^{46,47}

Affiliations are listed after the references.

Abstract

We present 29 successfully recovered CIV time lags in Active Galactic Nuclei from the complete Dark Energy Survey Reverberation Mapping campaign. The AGN in this sample span a redshift range of $1.9 < z < 3.5$. We successfully measure the velocity dispersion from the CIV spectral linewidth for 25 of these 29 sources, and use these to calculate new high-redshift black hole mass estimates, finding masses between 0.8 and 1.3 billion solar masses. We also identify a selection effect due to the duration of the survey that can impact the radius-luminosity relation derived from this and other (high-redshift) data. This paper represents the culmination of the OzDES CIV campaign.

Keywords: Active galactic nuclei, supermassive black holes.

(Received xx xx xxxx; revised xx xx xxxx; accepted xx xx xxxx)

1. Introduction

Supermassive black holes (SMBHs) are thought to exist in all large galaxies. These extreme objects, some of which appear to be more massive than ten billion solar masses (Wu et al. 2015; Onken et al. 2020; Eilers et al. 2023; Lai et al. 2023; Melo-Carneiro et al. 2025), act as tracers of cosmic history and as drivers of galaxy evolution. Understanding how the mass of these SMBHs grows over time offers insight into feedback during galaxy formation (Kormendy & Ho 2013), the properties of the first generation of stars, galaxy merger rates (Sahu et al. 2019), and the potential existence of primordial black holes (Volonteri et al. 2021).

Locally, the masses of SMBHs can be inferred from the kinematics of the material orbiting the black hole but, beyond the local universe, limits on the angular resolution of our

telescopes precludes the direct imaging of these dynamics.^a Instead, the dominant method of measuring SMBH mass beyond $z = 0.1$ is reverberation mapping (RM; Blandford & McKee 1982), a novel technique focusing on active galactic nuclei (AGN), which are SMBHs with active accretion disks.

In RM, long-term monitoring is carried out simultaneously for photometric and spectroscopic observations of a Seyfert-I galaxy, i.e. an AGN that exhibits broad emission lines. The accretion disk dominates the photometric observations, while the distinctive widening of the broad line region (BLR) emission lines allows its light to be identified via spectroscopy, and so we can track the variable activity of both regions independently. Variations in the accretion disk flux are ‘echoed’ in the variations of the broad line region, but with a lag associated with the time taken for the light to travel from the disk to the BLR, with a longer lag indicating a physically larger system. This ‘reverberation lag,’ identified by comparing the two light curves, allows us to use time-domain measurements as a spatial ruler.

RM is a time-domain technique that requires costly long-term observation campaigns, but it acts as the foundation for

^aAlthough Very Large Telescope Interferometer observations may enable us to probe the kinematics of the broad line region and measure the masses of especially massive black holes (Wolf et al. 2024).

Author for correspondence: Tamara Davis, Email: tamara.davis@physics.uq.edu.au

Cite this article: Penton et al., OzDES Reverberation Mapping Program: CIV lags from six years of data. *Publications of the Astronomical Society of Australia* 00, 1–12. <https://doi.org/10.1017/pasa.xxxx.xx>

the single-epoch method that requires only one measurement of an AGN’s luminosity and spectrum. The single epoch method is centred around the Radius-Luminosity ($R-L$) relationship, usually expressed as a power law, between the radius of the broad line region and the overall luminosity of the AGN.

The $R-L$ relation is currently best constrained for low-redshift hydrogen emission lines (e.g. $H\beta$ and $H\alpha$; Bentz et al. 2014). Much of the history of RM has focused on low-redshift AGN, using hydrogen emission lines for a small, focused sample of high signal-to-noise sources (e.g. Bentz et al. 2009). Such sources are limited in sample count and redshift, as sources beyond $z \approx 0.65$ are redshifted such that the $H\beta$ line falls outside the optical band. High energy reverberation emission lines have been investigated as alternatives for distant sources, including MgII at intermediate redshifts (e.g. Zajaček et al. 2020) and CIV for high-redshift sources (e.g. Kaspi et al. 2021b; Lira et al. 2018). RM with the CIV line has previously been investigated in low-redshift sources where the line appears in ultraviolet (UV) (Peterson et al. 2005; Metzroth et al. 2006; De Rosa et al. 2015). They found that the CIV lags are smaller than the lags measured from MgII or $H\beta$ by a factor of about two (Lira et al. 2018; Kaspi et al. 2007).

In the last decade, RM surveys have expanded to an ‘industrial scale’, in which hundreds to thousands of sources are observed out to high redshift. The Australian Dark Energy Survey (OzDES; Yuan et al. 2015; Childress et al. 2017; Lidman et al. 2020) contained one such industrial scale RM project, obtaining reverberation mapping measurements for 793 AGN in the redshift range $z \in [0.1, 3.8]$ over a 6-year period, with spectroscopy spanning the optical wavelength range of $\lambda \in [3750\text{\AA}, 8800\text{\AA}]$. OzDES acts as a contemporary counterpart to the Sloan Digital Sky Survey (SDSS; Shen et al. 2015), who released their final RM sample and analysis of over 1000 AGN sources in Shen et al. (2024).

This paper acts as an extension to the OzDES work with the CIV sample by Hoormann et al. (2019), and a companion to the OzDES MgII and $H\beta$ line analyses of Yu et al. (2023) and Malik et al. (2023). An upcoming paper will present the complete OzDES reverberation mapping sample, compare the results from the different lines, and merge with other data from the literature (McDougall et al. *prep*). In this work we present the CIV lags resulting from the full six years of monitoring. Our sources are drawn from the high-redshift ($1.6 < z < 4.5$) OzDES data. They are fit with the lag recovery program JAVELIN (Zu et al. 2011), which assumes the light curve follows a damped random walk and uses Markov chain Monte Carlo (MCMC) to recover the lag using a uniform lag prior (for details see McDougall et al. *prep*). We compare this result to an alternative method, the Interpolated Cross-Correlation Function (ICCF; Gaskell & Peterson 1987) as implemented in PyCCF (Sun et al. 2018). ICCF does a simple linear interpolation between data points and cross-correlates the photometric and spectroscopic light curves. Consistency between these methods is one of the criteria we use to identify high-quality lag recoveries. The resulting fits are subjected to stringent quality controls to remove contaminating false positives. In total, we find 29 CIV AGN lags, with these successful recoveries spanning the redshift range $1.9 < z < 3.5$.

The paper is structured as follows. In §2 we describe the observing program. In §3 we provide an overview of the properties of the 305 CIV sources that OzDES monitored and

outline the selection criteria we use to reduce false positives. In §4 we use the reverberation lags to constrain the central black hole masses for 25 of the sources (those for which we also successfully measured the CIV linewidth). In §5.1 we present an important selection bias that excludes long lags because of the limited duration of the survey, which can impact the derived radius-luminosity relation. In §6 we conclude and discuss the implications of these new mass estimates on the broader topic of SMBH demographics at high redshift.

2. Data and Sample Selection

Over the course of five years, DES imaged ten fields with approximately weekly cadence in the g, r, i, z bands, which OzDES followed up with spectroscopy at monthly cadence for six years (Lidman et al. 2020). DES imaging was performed on the CTIO Blanco 4-metre Telescope in Chile, while OzDES spectroscopy used the Anglo-Australian Telescope’s AAOmega spectrograph fed by the 2dF fibre positioner (for details see Lidman et al. 2020). While DES and OzDES were designed to discover supernovae and measure redshifts of their host galaxies, the program also had very good cadence for gathering AGN continuum light curves and spectroscopic response light curves needed for RM measurements. However, the seasonal observational window was not ideal for RM, with observations lasting roughly six months of the year for DES and five months for OzDES; this leaves large seasonal gaps in the RM light curves.

The 2dF instrument enables 400 spectra to be taken simultaneously, and about a quarter of its fibres were placed on AGN in each exposure. OzDES monitored a total of 771 AGN over six years (2013-2019), gathering between 18 and 25 epochs on each AGN with a spectral resolution of $1400 < R < 1700$ and a wavelength range of 3700\AA to 8800\AA . The images and catalogues from the whole DES survey are available at <https://des.ncsa.illinois.edu/releases/dr2>. The OzDES spectra are available from <https://docs.datacentral.org.au/ozdes/overview/dr2/>.

We use the calibration procedures outlined in Hoormann et al. (2019) for spectroscopic measurements. We take DES photometry in the g, r and i bands (discarding any of low quality, lacking adequate calibration, or outliers), and then average measurements that were taken on the same night. These are used to calibrate the OzDES spectra for each source, correcting for wavelength-dependent losses due the finite size of the fibres, and these calibrated spectra are then used to identify reverberating emission lines, their variations in strength for RM, and their velocity dispersions for SMBH mass estimates; see Hoormann et al. (2019) for more detail.

3. CIV Recovery Statistics

In total, there are 305 CIV sources in the DES/OzDES sample, although we expect only a fraction of them to provide recoverable lags. Based on projections made at the beginning of the OzDES campaign by King et al. (2015), we should expect between $\sim 20\%$ - 30% successful recoveries from the CIV sample due to a number of limiting factors. Firstly, only a fraction of the AGN are likely to vary significantly during the time of our observations. Secondly, the expected low signal-to-noise ratio in the OzDES data leads to large uncertainties in the

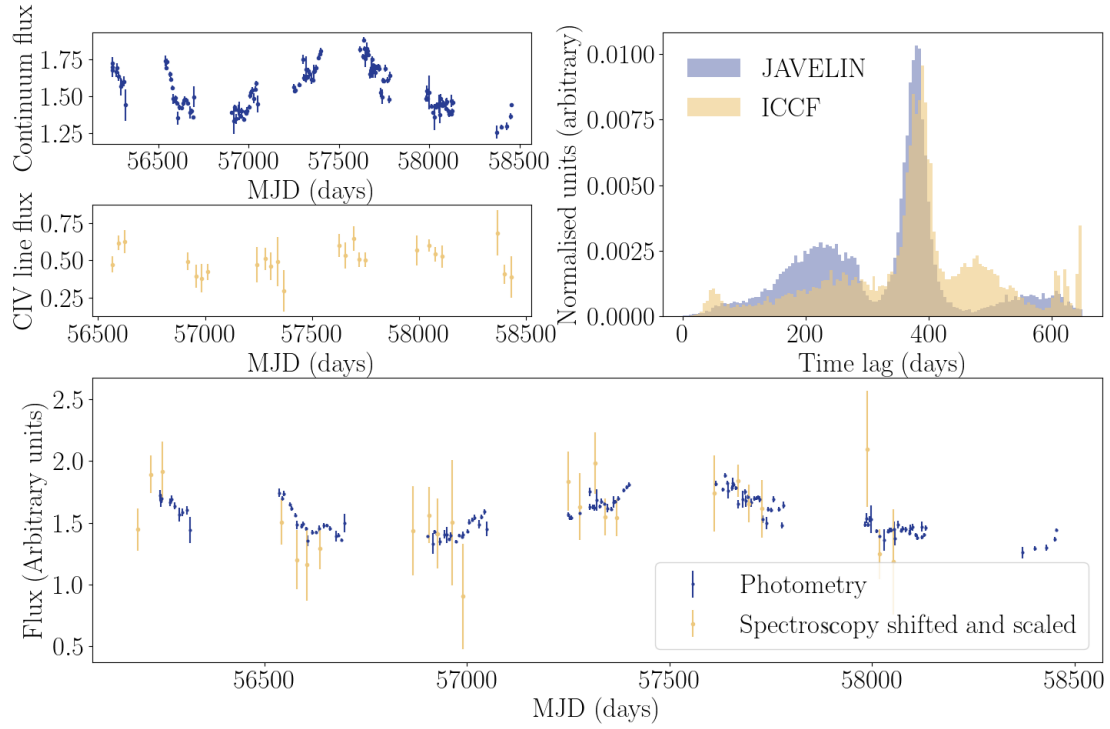


Figure 1. An example of gold rated source, DES J022620.86-045946.48. In the photometric and spectroscopic lightcurves we can see that there is a long term smooth variation that is present in both lightcurves. This is an important feature in most high quality lag measurements. This leads to a posterior for the lag (top right) with a sharp peak in both JAVELIN and ICCF. The smaller broader peaks at ~ 180 days and ~ 540 days correspond to seasonal gaps and are likely caused by aliasing.

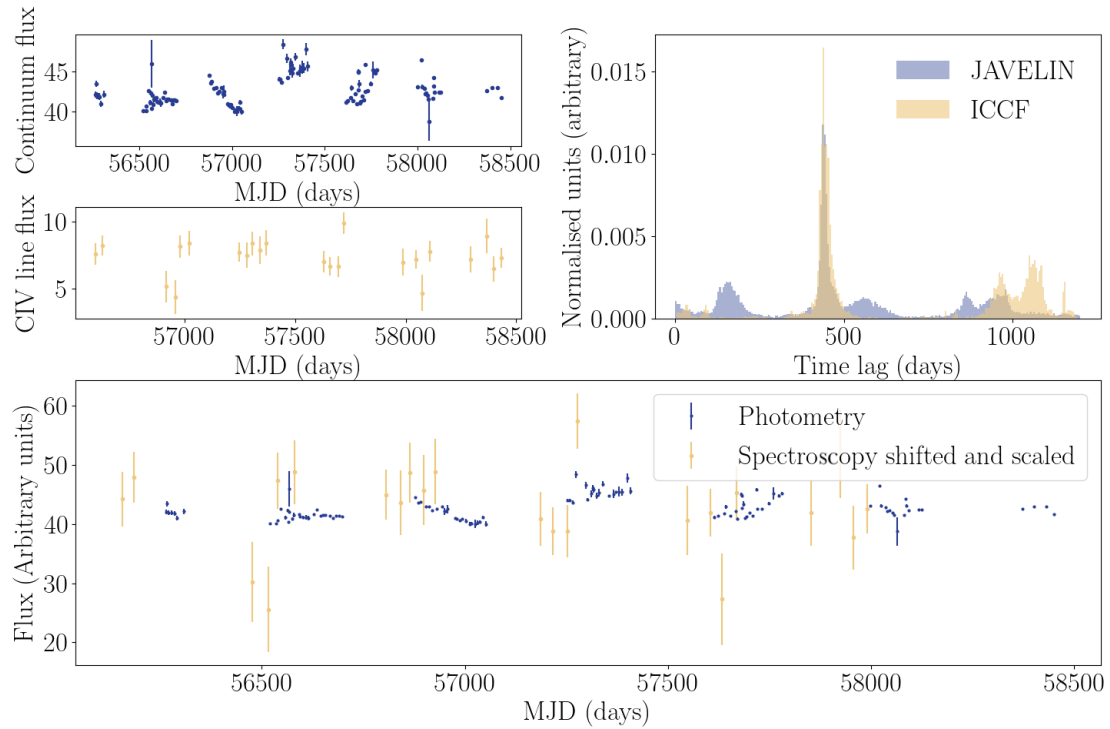


Figure 2. An example of silver rated source, DES J002959.21-434835.24. In the original photometric and spectroscopic lightcurves we can see that there is a long term variation present in the photometric lightcurve, however in this case there is a less obvious signal in the spectroscopic lightcurve. This leads to a posterior for the lag with a sharp peak in both JAVELIN and ICCF accompanied by many smaller peaks. These smaller peaks are likely caused by aliasing given their location, however, since there is much more of the probability contained within them, this example is rated as having a lower quality lag measurement than the example shown in Figure 1.

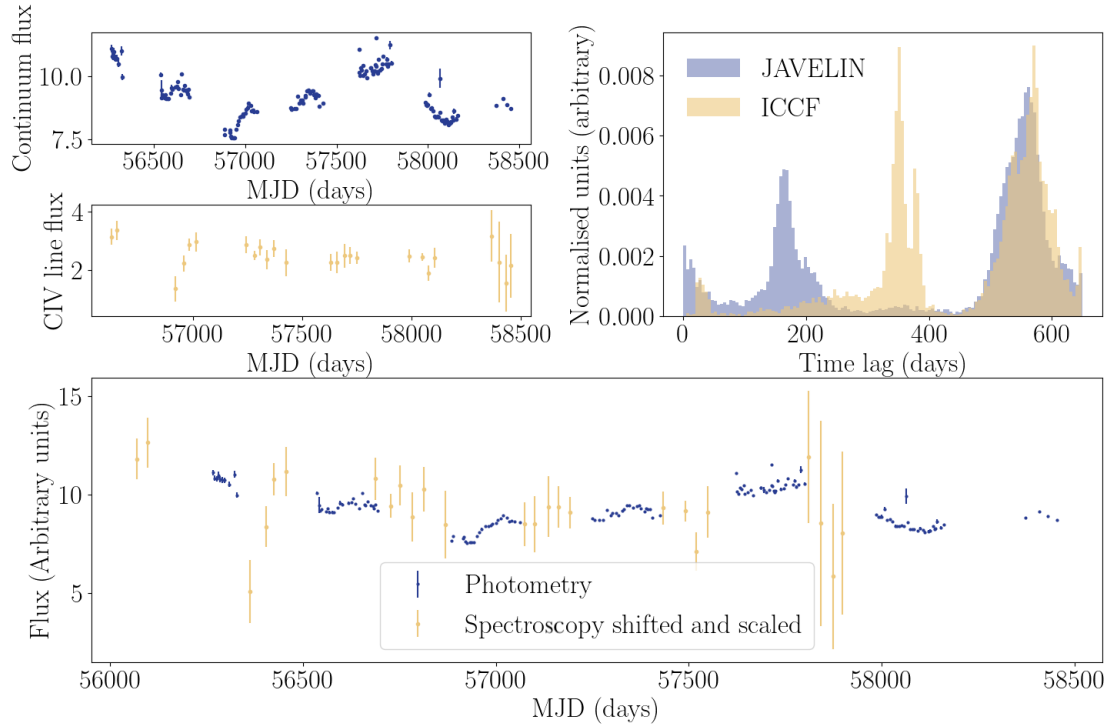


Figure 3. An example of bronze rated source, DES J032703.62-274425.27. In the photometric and spectroscopic lightcurves we can see that there is a variation in both lightcurves, however, with a generally lower signal-to-noise than seen in Figures 1 and 2, and very little temporal overlap due to seasonal gaps. This leads to a posterior for the lag with multiple sharp peaks in both JAVELIN and ICCF, however, the most prominent peak in both are the same, giving credibility to this measurement, albeit at lower confidence than the silver and gold samples.

individual measurements. Finally, the seasonal gaps in our observing cadence make some time delays difficult to recover, particularly those at half yearly intervals, e.g. 180 days, 540 days, etc. (Malik et al. 2022).

Using the quality cuts introduced in Penton et al. (2022), we ensure that we only select high-quality lag recoveries, which reduces the acceptance rate even further. In Table 1 we show the number of sources that pass each cut independently and cumulatively. For example, the second cut removes 174 sources if applied independently of the first cut. Detailed descriptions of the cuts can be found in Penton et al. (2022), but in summary:

1. The first cut removes the sources that either have broad and/or noisy posterior distributions that give them large uncertainties consistent with zero lag; this removes 50 sources.
2. The second cut is based on the disparity between measurements made using ICCF and JAVELIN. This is not a cut that is often made in the literature, however, simulations by Penton et al. (2022) showed it to be important; it removes another 145 sources.
3. The final pair of cuts splits the sample into bronze, silver, and gold. To make it into each sample both of the following criteria have to be passed to the appropriate level (as listed in Table 1).
 - a. Do the median and peak of the distribution agree to within a certain number of days?
 - b. Is there more than a certain percentage of the probability distribution in the primary peak?

		# Pass Each Cut Indep.	# Pass Each Cut Cumul.
All		305	305
Consistent with 0 at 3σ		255	255
$ \text{JAV.} - \text{ICCF} < 100$ days		131	110
Bronze	median–peak (< 110 days)	146	65
	% in peak ($> 33\%$)	85	29
Silver	median–peak (< 80 days)	127	57
	% in peak ($> 45\%$)	26	12
Gold	median–peak (< 65 days)	113	52
	% in peak ($> 60\%$)	13	6

Table 1. Number of sources that remain after each quality cut, both independently and cumulatively. Note that the pairs of cuts for gold, silver and bronze indicate the number that pass, firstly, only the cut on the difference between median and peak lag (median–peak), and secondly, *both* the median–peak and the peak proportion cuts for that rating.

These latter criteria penalise sources that have significant likelihood outside the primary (highest) peak.^b We show three examples of recoveries, one each for gold, silver, and bronze, in Figure 1 to Figure 3. These cuts result in 6 gold-standard sources, 6 silver, and 17 bronze. The simulations in Penton et al. (2022) show that gold, silver, and bronze all represent high-quality lags — the mean offset from the true lag ranges from 13 days (gold) to 18 days (bronze) and the false detection percentage ranges from 12% (gold) to 19% (bronze).

^bWe identify the highest peak and integrate the probability distribution between the local minima on either side of the peak.

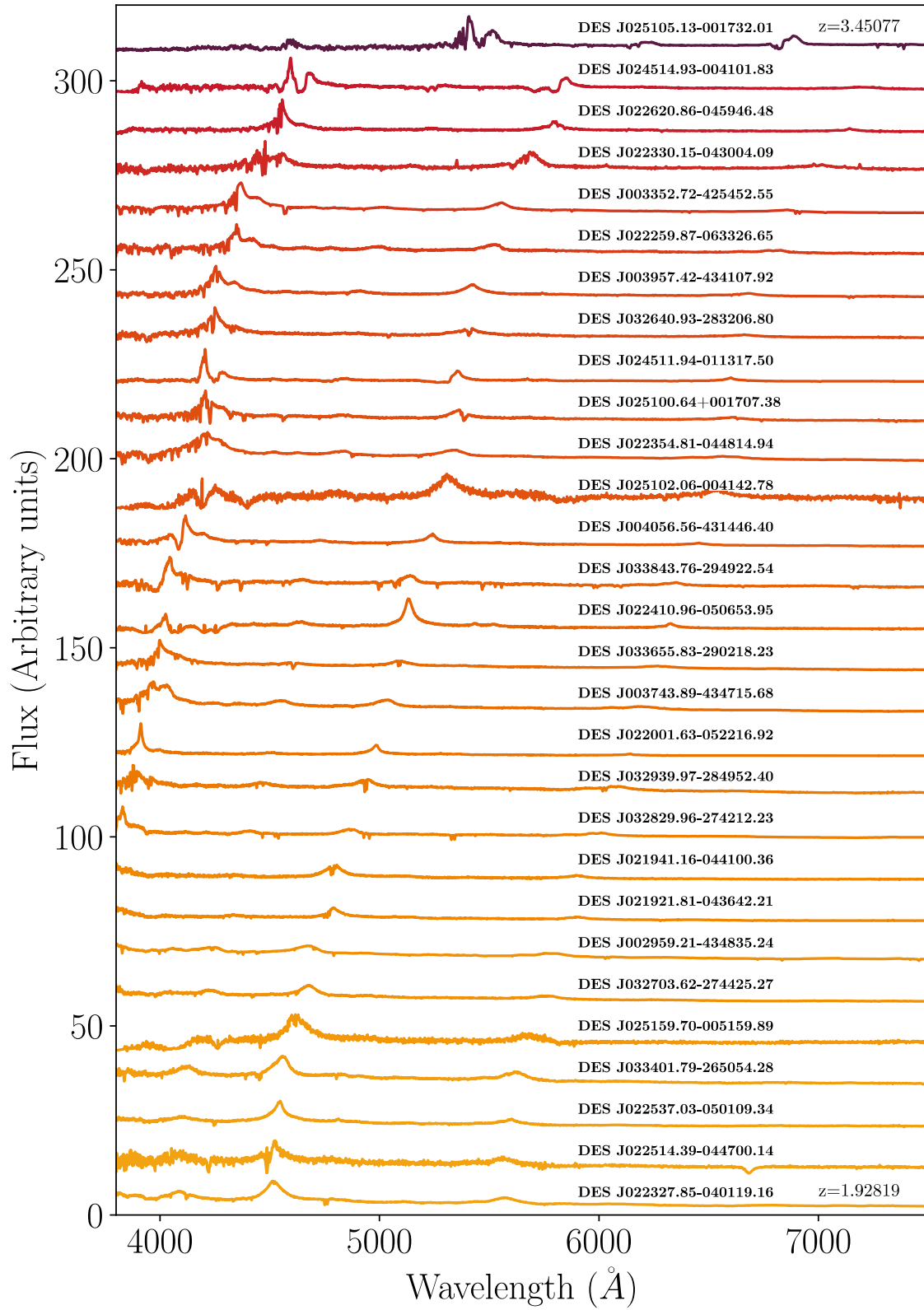


Figure 4. Spectra for all successfully recovered CIV sources. Note that the OzDES spectrum spans the wavelength range 3800-8800Å, however, for visibility the plotting range has been restricted to 3800-7500Å. The CIV line appears at $\sim 4537\text{Å}$ in the lowest redshift source and progresses toward the right as redshift increases (darker red indicates higher redshift). Some spectra show absorption features in the CIV line, which were severe enough in four sources to prevent an accurate linewidth measurement (see Table 2).

3.1. Potential for Increased Recovery Rate

The cut that has the biggest impact on the final number of recovered sources is the cut on the proportion of the lag posterior contained within the peak of the posterior (only 85 of the 305 AGN pass this criterion at the Bronze level). Given that we find that sources observed at higher redshifts often have lower signal-to-noise due to observational limitations, it is not surprising that a high-redshift sample would contain a significant number of low SNR posterior lag distributions.

When measuring high quality black hole masses, a strict cut on this parameter is necessary, though it may be possible to instead use this information on a sliding scale. The proportion in the peak gives a measure of the level of noise and aliasing in the posterior distribution, i.e. the more artefacts in the signal the lower the prominence of the primary peak in comparison. Effectively we get increasingly certain of the results as the peak prominence increases; this means that if treated correctly with weighting or uncertainty scaling it may be possible to use all the sources that pass the other cuts, and use the percentage in the peak as a weighting for the confidence of the lag recovery. If possible this would enable the use of 65 sources, over double the number that are presented in this paper.

4. Recovering Black Hole Masses

Having collated a high quality set of 29 time lags, we can now use them to measure the masses of their associated black holes. To compute a black hole mass we use the virial equation:

$$M_{\text{BH}} = f \frac{c t_{\text{lag}} \Delta V^2}{G}, \quad (1)$$

where t_{lag} denotes the time lag between the central SMBH and the BLR, so that ct_{lag} is an estimate of the BLR radius; ΔV denotes the BLR velocity dispersion as measured from the reverberating emission line; and f represents the ‘virial factor,’ an empirical correction factor that accounts for the mean kinematic properties of all AGN including unknown inclination, internal kinematics, and other undetermined properties of the internal regions of the AGN. Multiple estimates for the virial factor are discussed in the literature, based on different data sets and different methodologies. In this work, we use the virial factor of $f = 4.47 \pm 1.1$ based on the work by Woo et al. (2015), as it is the most widely used – however, it is important to note that this was derived based on measurements for $\text{H}\beta$. The uncertainty on this measurement is quite large, often being the dominant source of uncertainty in the mass measurements.

To measure the BLR velocity dispersion for each source we measure the linewidth of the C IV line. All 29 AGN with measured CIV lags are shown in Figure 4. This is done by measuring the linewidth of the mean spectrum; however, this does come with limitations. There is some evidence showing that there are non-negligible contributions from outflows in the line profile of some C IV sources. Denney (2012) showed that high velocity outflows from the central region of AGN may cause widening on the blue side of the C IV line. This widening would make linewidth measurements using the mean spectrum possibly inaccurate since these outflows are not part of the orbital motion of the BLR clouds. This could be mitigated by using the RMS of the spectrum, thus showing only the parts

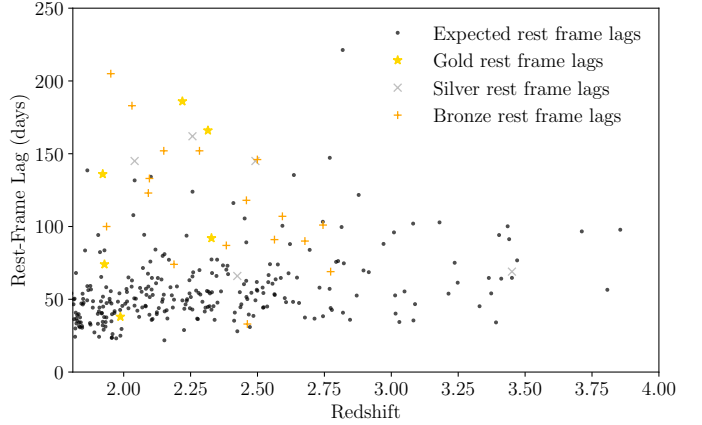


Figure 5. The distribution of recovered rest frame lags and redshifts compared to the expected distribution of the OzDES sample based on historic $R - L$ relation estimates (Grier et al. 2019). Note that it appears to be difficult to recover lags above a redshift $z = 2.8$, with only one recovery out of a possible ~ 30 , with no gold measurements above $z = 2.35$. This is likely due to low intrinsic variability of high-luminosity sources, the low signal-to-noise of high-redshift measurements, and time limit due to the maximum survey duration.

of the line profile that are changing with time. Unfortunately, the signal-to-noise ratio of the OzDES spectra are insufficient to reliably measure linewidths of the RMS spectrum. However, the effect of outflows is not always present nor does it cause a systemic bias in one direction (Denney 2012). This means that, for considering the behaviour of the sample, it would only have an effect of increasing the intrinsic scatter in black hole masses. For single epoch mass measurements, the majority of the outflows that have been observed cause shifts of less than 1σ in the velocity measurement. Therefore, this effect would be sub-dominant to the uncertainties in the virial factor and the lag uncertainty.

Our 25 black hole mass measurements are presented in Table 2. While smaller in number than the 110 CIV lags presented in Shen et al. (2024), our stringent selection criteria mean that this sample is very robust. We find an intrinsic scatter in our radius-luminosity relation 2.5 times smaller than that in the SDSS sample (~ 0.2 dex vs ~ 0.5 dex); see Figure 7 of McDougall et al. (prep).

To assess how supermassive black holes have evolved over cosmic time we will require many more sources. To achieve this, McDougall et al. (in prep) will leverage the results presented here to measure black hole masses of a larger sample. While we have only a limited number of reverberation mapped sources, there are thousands of AGN in the OzDES catalogue for which we have photometry and spectroscopy, just not over as long a time period. All of these represent a possible black hole mass measurement using the $R - L$ relation combined with a single-epoch spectroscopic velocity measurement. Future analyses will be able to apply these $R - L$ relations to even larger samples, such as those from SDSS, the Dark Energy Spectroscopic Instrument (DESI), and 4MOST (Swann et al. 2019).

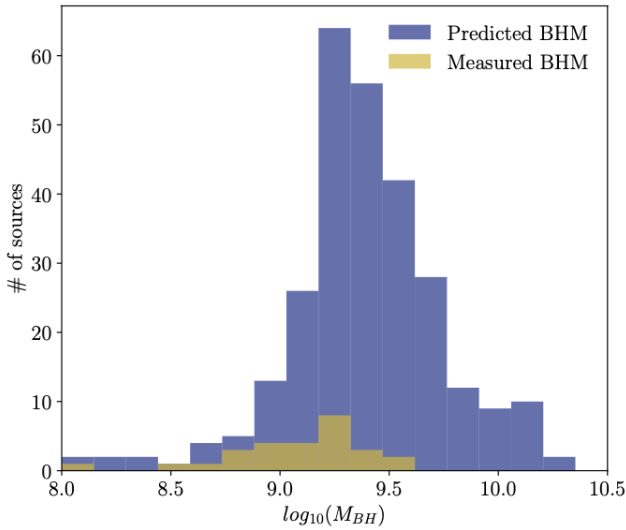


Figure 6. A comparison of the distribution of predicted black hole masses with the distribution of measured black hole masses (in units of solar mass). Note the generally smaller masses of the black holes that had successful measurements (gold) relative to the input sample (purple).

5. Selection effects, demographics, and the $R - L$ relation

In order to infer properties of the population of AGN as a function of redshift, one needs to consider the selection effects that impact the sample. The selection effects occur at two stages. Firstly, did OzDES observe a representative sample of AGN? Secondly, of the observed AGN, which had successful lags?

As a means of contrasting our mass measurements with a priori estimates, we use an $R - L$ relation from the literature (Grier et al. 2019) to predict time lags for our entire sample, and combine that with the measured velocity dispersion, to give an estimate of the black hole mass. This allows us to estimate the distribution of lags and SMBH masses that are expected for the OzDES sample.^c In Figure 5 we compare the 29 measured lags with the predicted lags for the entire sample inferred from the $R - L$ relation. We see the bulk of our successful CIV lag recoveries lie at low redshift and high rest-frame lag. There are several reasons for this:

- **Cadence and Seasonal Gaps:** The lack of recoveries at lower rest-frame lags can occur because short lags are difficult to constrain reliably given the monthly cadence of our observations, and the 6-8 month gaps between seasons. As discussed in Malik et al. (2022), filling in the seasonal gaps increases the chances of successfully measuring lags.
- **Survey duration:** Time dilation lengthens the observer-frame duration of lags, which makes it difficult to observe very long lags at high redshift, as observed lags can become longer than the maximum duration of the survey. This has an important impact on the $R - L$ relation (see Section 5.1).
- **Variability time scale:** Sources with longer lags indicate a larger BLR, which is generally correlated with longer-term variability (Lu et al. 2019; Tarrant et al. 2025),

^cTo derive lags, Grier et al. (2019) use the variations of luminosity $\log \lambda L_{\lambda}(1350\text{\AA})$ in erg s^{-1} compared to the variability of the RMS spectrum of CIV.

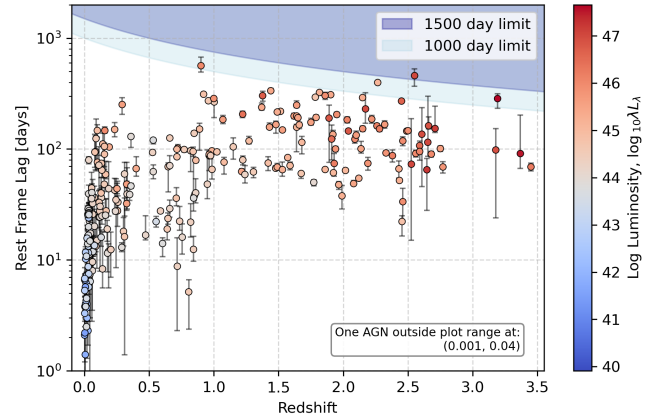


Figure 7. Compilation of data from the literature and this paper, showing rest-frame lags as a function of redshift, and coloured by the luminosity of the AGN. Shading shows the approximate upper limit of possible lag recoveries given typical survey durations (observer-frame lags of 1000 and 1500 days). There is a decrease in the highest measurable rest-frame lag as redshift increases. This impacts CIV measurements the most, and is an important selection effect for the CIV $R - L$ relation (see Figure 8). Data are from the compilation in McDougall et al. (prep), which includes the DES CIV measurements from this paper.

meaning they can be constrained even when there are large gaps in the data.

- **Variability amplitude:** Smaller black holes, contained within lower luminosity AGN, tend to be more variable sources. These sources will have lightcurves with higher variability and would therefore be more likely to be recovered.
- **Signal-to-noise:** High-redshift targets tend to have lower signal-to-noise than low-redshift targets.

These selection effects can be seen in our black hole mass distribution. In Figure 6 we show a histogram of the black hole masses that we have measured through RM compared to those predicted by the $R - L$ relation. This comparison shows that, on average, OzDES successfully recovered lags primarily for the sources with low black hole masses. This is primarily due to the smaller black holes having higher variability, and larger black holes hitting the duration limit of the survey (see Section 5.1).

Both of these reasons are selection effects, and are likely not indicative of individual black holes being less massive than expected. However, this does indicate that it is difficult to measure the very large black hole masses above $10^{10} M_{\odot}$ with the survey structure and length of OzDES. A longer baseline and/or deeper spectroscopy would be required to measure these gargantuan black holes.

One final feature of importance is that many of the CIV observer-frame lags are expected to be in seasonal gaps, because at $2 \lesssim z \lesssim 3$ time dilation shifts a rest-frame lag of 50 days to ~ 150 to 200 days in the observer frame. We found that current lag recovery methods may be overly sensitive to aliasing effects due to seasonal gaps in the light curves. In future work we aim to use the new LITMUS program to do AGN reverberation mapping (McDougall et al. 2025), as this significantly improves on JAVELIN's method of exploring the parameter space, reducing the impact of aliasing.

5.1. Selection Effects' Impact on the Radius-Luminosity Relation

Measuring black hole masses is only one of the applications of this data set. In addition we can construct a scaling relation based on the measured radius of the broad line region and the luminosity of the AGN. In McDougall et al. (*prep*) we re-derive the $R-L$ relation for all emission lines used by OzDES, so we defer to that paper for the new CIV $R-L$ relation both from OzDES and in combination with existing surveys.^d

Here we look at one important feature of the CIV sample that impacts the $R-L$ relation, namely the selection effect that arises due to survey duration. The observed duration of events is time-dilated by a factor of $1+z$ relative to the duration at emission (recent measurements from quasars and DES supernovae respectively include Lewis & Brewer 2023; White et al. 2024). Therefore, a lag of one year in the rest frame would appear as three years for a $z=2$ object. Due to the high redshift of the CIV sample, it is more affected by time-dilation than H β or MgII.

While exploring the $R-L$ relation in Penton (2023), we discovered a discrepancy between the $R-L$ relation constructed using the literature data points and that using only the data from this work. At first glance it appears that the high-luminosity sample of OzDES has a shallower slope than the literature data that extend to lower luminosities. There are multiple possible reasons for this distinction between low and high luminosity regimes. The first possibility is that there is an intrinsic difference between the sources in the different regimes. If there were an evolutionary difference between the populations this could cause the disparity in the relations. On the other hand, there are possible observational biases that would prevent recoveries in certain parts of the $R-L$ relation. For example, if time lags on certain time scales are less likely to be successfully recovered, this could skew the $R-L$ relation. It is this selection effect we believe to be at play in the OzDES data.

In Figure 7 we plot lag vs redshift, colour coding the points by their luminosity. For this plot we include high-quality data from the literature as compiled in our companion paper (McDougall et al. *prep*), including data from H β and MgII lines (Peterson et al. 2005; Rosa et al. 2015; Grier et al. 2019; Kaspi et al. 2021a; Shen et al. 2024). It is clear that higher luminosities tend to come from sources at higher redshifts.

A ramification of this can also be seen in Figure 7, where we draw contours of the approximate rest-frame lags that can be measured as a function of redshift. One cannot recover a lag longer than the survey duration, and ideally one wants the observing window to be significantly longer than the lag. So these contours (at 1000 and 1500 days in the observer frame) act as approximate upper limits to the lags we could detect (OzDES spanned approximately 2150 days from the first to last observation).

This is compounded at high redshift by the fact that high-luminosity sources also have intrinsically longer lags (as seen in the $R-L$ relation). The cutoffs in Figure 7 can therefore be

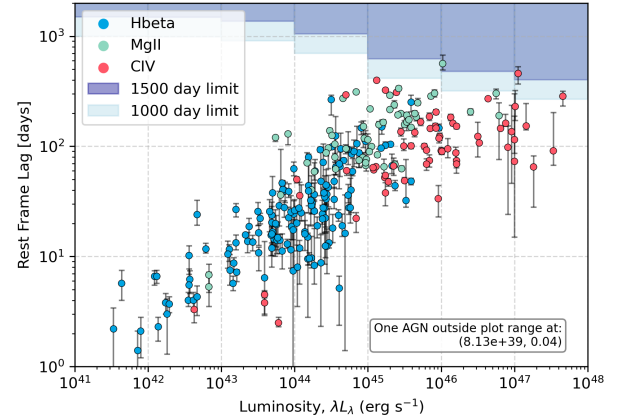


Figure 8. Compilation of data from the literature and this paper, showing rest frame lag vs luminosity. Shaded regions show the estimated upper limit of possible recoveries given the duration of typical large-scale surveys (averaging the limit shown in Figure 7 in luminosity bins). Note that at higher luminosities ($L \gtrsim 10^{46} \text{ erg s}^{-1}$) the areas that are excluded due to survey duration start to impact regions where we expect data. Thus there may be a bias towards points on the lower side of the $R-L$ relation at higher luminosities.

translated into cutoffs that could adversely affect the $R-L$ relation. Since there is not a direct correlation between luminosity and redshift, we have binned the data into 7 luminosity bins, calculating the average ‘maximum lag’ measurable for the AGN in each of those bins. The result of this can be seen in Figure 8.

There is a clear ceiling where one would expect to see longer duration lags, but they are not detectable because the duration of the survey was insufficient to see the very delayed spectral response to the continuum variation. This is an important selection effect we need to correct for when deriving the $R-L$ relationship for CIV (see McDougall et al. *prep*).

Moving into the future, this bias will need to be carefully parameterised if we are to accurately derive the $R-L$ relation using even larger samples of high-redshift data. One can mitigate this effect by extending RM surveys to longer observational baselines, enabling them to recover longer rest-frame lags successfully. Such data will be necessary to conclusively rule out a flattening of the slope of the CIV $R-L$ relation. Notably, the DES supernova fields we used this AGN monitoring campaign continue to be monitored with DECam by the HELM program (Zhuang et al. 2024), resulting in a photometric sequence that spans more than a decade.

6. Conclusions

We recover 29 high-quality CIV lags from observing 305 AGN over six years with weekly photometric cadence and monthly spectroscopic cadence with the DES/OzDES program. Using these lags in combination with linewidth velocity dispersion measurements, we measure masses of the central supermassive black holes for 25 of these AGN.

We note that selection effects impact the demographics of the AGN in this sample, which occupies the upper edges of our survey’s window function in redshift-luminosity space. Seasonal gaps and the total length of the survey are limiting factors in RM lag recovery, particularly at high redshift where

^dIn an early version of this work, which appears in the thesis of the lead author (Penton 2023), you can find some additional analyses that include a preliminary CIV $R-L$ relation, and an analysis including an additional 65 OzDES AGN measurements weighted by the proportion of their posterior contained within the primary likelihood peak.

observed lags and timescales of variations are longer. In particular, we identify that building an $R - L$ relationship for the CIV line requires one to take into account the selection effect that the duration of the survey imposes on the maximum recoverable lag.

Future surveys may allow us to probe different regions of luminosity-redshift space, providing more reliable anchors for the $R - L$ relationship. Industrial-scale surveys such as OzDES offer a wealth of sources. With the high inherent scatter and the difficulty in constraining the $R - L$ relationship for CIV, there is good motivation to improve the breadth and density of CIV RM sources to properly characterise this behaviour.

Contribution Statement

Project conception and coordination: TMD, CL, PM; Analysis, programming, calculations: AP, ZY, HM; Writing: AP, HM, TMD; Figures: AP, TMD; Editing: CL, PM, ZY, RS; Data generation and/or curation: all authors.

Acknowledgements

AP, UM, and HM are supported by the Australian Government Research Training Program (RTP) Scholarship. TMD acknowledges support for early stages of this project from an Australian Research Council (ARC) Laureate Fellowship (project number FL180100168) and for later stages from the ARC Centre of Excellence for Gravitational Wave Discovery, OzGrav (CE230100016). PM and ZY were supported in part by the United States National Science Foundation under Grant No. 161553 to PM. PM also acknowledges support from the United States Department of Energy, Office of High Energy Physics under Award Number DE-SC-0011726.

Parts of this research were carried out on the traditional lands of the Ngannawal and Ngambri peoples. This work makes use of data acquired at the Anglo-Australian Telescope, under program A/2013B/012. We acknowledge the Gamilaraay people as the traditional owners of the land on which the AAT stands. We pay our respects to their elders past, present, and emerging.

This analysis used NUMPY (Harris et al. 2020), ASTROPY (Astropy Collaboration et al. 2013, 2018), and SCIPY (Virtanen et al. 2020). Plots were made using MATPLOTLIB (Hunter 2007). This work has made use of the SAO/NASA Astrophysics Data System Bibliographic Services.

Funding for the DES Projects has been provided by the U.S. Department of Energy, the U.S. National Science Foundation, the Ministry of Science and Education of Spain, the Science and Technology Facilities Council of the United Kingdom, the Higher Education Funding Council for England, the National Center for Supercomputing Applications at the University of Illinois at Urbana-Champaign, the Kavli Institute of Cosmological Physics at the University of Chicago, the Center for Cosmology and Astro-Particle Physics at the Ohio State University, the Mitchell Institute for Fundamental Physics and Astronomy at Texas A&M University, Financiadora de Estudos e Projetos, Fundação Carlos Chagas Filho de Amparo à Pesquisa do Estado do Rio de Janeiro, Conselho Nacional de Desenvolvimento Científico e Tecnológico and the Ministério da Ciência, Tecnologia e Inovação, the Deutsche Forschungsgemeinschaft and the Collaborating Institutions in the Dark Energy Survey.

The Collaborating Institutions are Argonne National Laboratory, the University of California at Santa Cruz, the University of Cambridge, Centro de Investigaciones Energéticas, Medioambientales y Tecnológicas-Madrid, the University of Chicago, University College London, the DES-Brazil Consortium, the University of Edinburgh, the Eidgenössische Technische Hochschule (ETH) Zürich, Fermi National Accelerator Laboratory, the University of Illinois at Urbana-Champaign, the Institut de Ciències de l'Espai (IEEC/CSIC), the Institut de Física d'Altes Energies, Lawrence Berkeley National Laboratory, the Ludwig-Maximilians Universität München and the associated Excellence Cluster Universe, the University of Michigan, NSF NOIRLab, the University of Nottingham, The Ohio State University, the University of Pennsylvania, the University of Portsmouth, SLAC National Accelerator Laboratory, Stanford University, the University of Sussex, Texas A&M University, and the OzDES Membership Consortium.

Based in part on observations at NSF Cerro Tololo Inter-American Observatory at NSF NOIRLab (NOIRLab Prop. ID 2012B-0001; PI:

J. Frieman), which is managed by the Association of Universities for Research in Astronomy (AURA) under a cooperative agreement with the National Science Foundation.

The DES data management system is supported by the National Science Foundation under Grant Numbers AST-1138766 and AST-1536171. The DES participants from Spanish institutions are partially supported by MICINN under grants PID2021-123012, PID2021-128989 PID2022-141079, SEV-2016-0588, CEX2020-001058-M and CEX2020-001007-S, some of which include ERDF funds from the European Union. IFAE is partially funded by the CERCA program of the Generalitat de Catalunya. We acknowledge support from the Brazilian Instituto Nacional de Ciência e Tecnologia (INCT) do e-Universo (CNPq grant 465376/2014-2). This document was prepared by the DES Collaboration using the resources of the Fermi National Accelerator Laboratory (Fermilab), a U.S. Department of Energy, Office of Science, Office of High Energy Physics HEP User Facility. Fermilab is managed by Fermi Forward Discovery Group, LLC, acting under Contract No. 89243024CSC000002.

References

- Astropy Collaboration et al., 2013, [A&A](#), **558**, A33
- Astropy Collaboration et al., 2018, [AJ](#), **156**, 123
- Bentz M. C., Peterson B. M., Netzer H., Pogge R. W., Vestergaard M., 2009, [ApJ](#), **697**, 160
- Bentz M. C., et al., 2014, [ApJ](#), **796**, 8
- Blandford R. D., McKee C. F., 1982, [ApJ](#), **255**, 419
- Childress M. J., et al., 2017, [MNRAS](#), **472**, 273
- De Rosa G., et al., 2015, [ApJ](#), **806**, 128
- Denney K. D., 2012, [ApJ](#), **759**, 44
- Eilers A.-C., et al., 2023, [ApJ](#), **950**, 68
- Gaskell C. M., Peterson B. M., 1987, [ApJS](#), **65**, 1
- Grier C. J., et al., 2019, [ApJ](#), **887**, 38
- Harris C. R., et al., 2020, [Nature](#), **585**, 357
- Hoormann J. K., et al., 2019, [MNRAS](#), **487**, 3650
- Hunter J. D., 2007, [Computing in Science & Engineering](#), **9**, 90
- Kaspi S., Brandt W. N., Maoz D., Netzer H., Schneider D. P., Shemmer O., 2007, [ApJ](#), **659**, 997
- Kaspi S., Brandt W. N., Maoz D., Netzer H., Schneider D. P., Shemmer O., Grier C. J., 2021a, Taking a Long Look: A Two-Decade Reverberation Mapping Study of High-Luminosity Quasars ([arXiv:2106.00691](#))
- Kaspi S., Brandt W. N., Maoz D., Netzer H., Schneider D. P., Shemmer O., Grier C. J., 2021b, [ApJ](#), **915**, 129
- King A. L., et al., 2015, [MNRAS](#), **453**, 1701
- Kormendy J., Ho L. C., 2013, [Annual Review of Astronomy and Astrophysics](#), **51**, 511–653
- Lai S., Wolf C., Onken C. A., Bian F., 2023, [MNRAS](#), **521**, 3682
- Lewis G. F., Brewer B. J., 2023, [Nature Astronomy](#), **7**, 1265
- Lidman C., et al., 2020, [MNRAS](#), **496**, 19–35
- Lira P., et al., 2018, [ApJ](#), **865**, 56
- Lu K.-X., et al., 2019, [ApJ](#), **877**, 23
- Malik U., et al., 2022, [MNRAS](#), **516**, 3238
- Malik U., et al., 2023, [MNRAS](#), **520**, 2009
- McDougall H. G., Davis T. M., Pope B. J. S., 2025, [arXiv e-prints](#), [p. arXiv:2505.09832](#)
- McDougall H. G., Davis T. M., Lidman C., Martini P., Yu Z., in prep., OzDES Reverberation Mapping of Active Galactic Nuclei: Final Data Release, Single Epoch Constraints & Black-Hole Mass Results
- Melo-Carneiro C. R., Collett T. E., Oldham L. J., Enzi W. J. R., Furlanetto C., Chies-Santos A. L., Li T., 2025, [arXiv e-prints](#), [p. arXiv:2502.13788](#)
- Metzroth K. G., Onken C. A., Peterson B. M., 2006, [ApJ](#), **647**, 901
- Onken C. A., Bian F., Fan X., Wang F., Wolf C., Yang J., 2020, [MNRAS](#), **496**, 2309
- Penton A., 2023, PhD thesis, [doi:https://doi.org/10.14264/25a5414](https://doi.org/10.14264/25a5414), <https://espace.library.uq.edu.au/view/UQ:25a5414>
- Penton A., et al., 2022, [MNRAS](#), **509**, 4008

Peterson B. M., et al., 2005, *The Astrophysical Journal*, 632, 799–808
 Rosa G. D., et al., 2015, *The Astrophysical Journal*, 806, 128
 Sahu N., Graham A. W., Davis B. L., 2019, *ApJ*, 876, 155
 Shen Y., Brandt W. N., Dawson K. S., Hall P. B., McGreer, et al I. D., 2015, *ApJS*, 216, 4
 Shen Y., et al., 2024, *ApJS*, 272, 26
 Sun M., Grier C. J., Peterson B. M., 2018, PyCCF: Python Cross Correlation Function for reverberation mapping studies, Astrophysics Source Code Library (ascl:1805.032)
 Swann E., et al., 2019, *The Messenger*, 175, 58
 Tarrant A., et al., 2025, The AGN Optical Variability Fundamental Plane ([arXiv:2501.12444](https://arxiv.org/abs/2501.12444)), <https://arxiv.org/abs/2501.12444>
 Virtanen P., et al., 2020, *Nature Methods*, 17, 261
 Volonteri M., Habouzit M., Colpi M., 2021, *Nature Reviews Physics*, 3, 732–743
 White R. M. T., et al., 2024, *MNRAS*, 533, 3365
 Wolf C., Lai S., Onken C. A., Amrutha N., Bian F., Hon W. J., Tisserand P., Webster R. L., 2024, *Nature Astronomy*, 8, 520
 Woo J.-H., Yoon Y., Park S., Park D., Kim S. C., 2015, *ApJ*, 801, 38
 Wu X.-B., et al., 2015, *Nature*, 518, 512
 Yu Z., et al., 2023, *MNRAS*, 522, 4132–4147
 Yuan F., et al., 2015, *MNRAS*, 452, 3047
 Zajaček M., et al., 2020, *ApJ*, 896, 146
 Zhuang M.-Y., et al., 2024, *ApJS*, 274, 42
 Zu Y., Kochanek C. S., Peterson B. M., 2011, *ApJ*, 735, 80

Affiliations

¹School of Mathematics and Physics, University of Queensland, Brisbane, QLD 4072, Australia, ²Kavli Institute for Particle Astrophysics & Cosmology, P. O. Box 2450, Stanford University, Stanford, CA 94305, USA, ³The Research School of Astronomy and Astrophysics, Australian National University, ACT 2601, Australia, ⁴Center for Cosmology and Astro-Particle Physics, The Ohio State University, Columbus, OH 43210, USA, ⁵Department of Astronomy, The Ohio State University, Columbus, OH 43210, USA, ⁶Centre for Gravitational Astrophysics, College of Science, The Australian National University, ACT 2601, Australia, ⁷Sydney Institute for Astronomy, School of Physics, A28, The University of Sydney, NSW 2006, Australia, ⁸INAF-Osservatorio Astronomico di Trieste, via G. B. Tiepolo 11, I-34143 Trieste, Italy, ⁹Laboratório Interinstitucional de e-Astronomia - LIneA, Av. Pastor Martin Luther King Jr, 126 Del Castilho, Nova América Offices, Torre 3000/sala 817, Brazil, ¹⁰Fermi National Accelerator Laboratory, P. O. Box 500, Batavia, IL 60510, USA, ¹¹Physik-Institut, University of Zürich, Winterthurerstrasse 190, CH-8057 Zürich, Switzerland, ¹²Departamento de Física Teórica, Centro de Astropartículas y Física de Altas Energías (CAPA), Universidad de Zaragoza, 50009 Zaragoza, Spain, ¹³Institute of Cosmology and Gravitation, University of Portsmouth, Portsmouth, PO1 3FX, UK, ¹⁴University Observatory, LMU Faculty of Physics, Scheinerstr. 1, 81679 Munich, Germany, ¹⁵Department of Physics & Astronomy, University College London, Gower Street, London, WC1E 6BT, UK, ¹⁶Instituto de Astrofísica de Canarias, E-38205 La Laguna, Tenerife, Spain, ¹⁷Universidad de La Laguna, Dpto. Astrofísica, E-38206 La Laguna, Tenerife, Spain, ¹⁸Korea Astronomy and Space Science Institute, 776 Daedeok-daero, Yuseong-gu, Daejeon 34055, South Korea, ¹⁹Institut de Física d'Altes Energies (IFAE), The Barcelona Institute of Science and Technology, Campus UAB, 08193 Bellaterra (Barcelona) Spain, ²⁰Kapteyn Astronomical Institute, University of Groningen, Landleven 12 (Kapteynborg, 5419), 9747 AD Groningen, The Netherlands, ²¹Hamburger Sternwarte, Universität Hamburg, Gojenbergsweg 112, 21029 Hamburg, Germany, ²²Centro de Investigaciones Energéticas, Medioambientales y Tecnológicas (CIEMAT), Madrid, Spain, ²³Department of Physics, IIT Hyderabad, Kandi, Telangana 502285, India, ²⁴California Institute of Technology, 1200 East California Blvd, MC 249-17, Pasadena, CA 91125, USA, ²⁵Instituto de Física Teórica UAM/CSIC, Universidad Autónoma de Madrid, 28049 Madrid, Spain, ²⁶Centre for Astrophysics & Supercomputing, Swinburne University of Technology, Victoria 3122, Australia, ²⁷Santa Cruz Institute for Particle Physics, Santa Cruz,

CA 95064, USA, ²⁸Department of Physics, The Ohio State University, Columbus, OH 43210, USA, ²⁹Lowell Observatory, 1400 Mars Hill Rd, Flagstaff, AZ 86001, USA, ³⁰Jet Propulsion Laboratory, California Institute of Technology, 4800 Oak Grove Dr., Pasadena, CA 91109, USA, ³¹Department of Physics and Astronomy, University of Pennsylvania, Philadelphia, PA 19104, USA, ³²George P. and Cynthia Woods Mitchell Institute for Fundamental Physics and Astronomy, and Department of Physics and Astronomy, Texas A&M University, College Station, TX 77843, USA, ³³Université Grenoble Alpes, CNRS, LPSC-IN2P3, 38000 Grenoble, France, ³⁴Institució Catalana de Recerca i Estudis Avançats, E-08010 Barcelona, Spain, ³⁵Department of Astrophysical Sciences, Princeton University, Peyton Hall, Princeton, NJ 08544, USA, ³⁶Centro de Tecnologia da Informação Renato Archer, Campinas, SP, Brazil - 13069-901, ³⁷Observatório Nacional, Rua Gal. José Cristino 77, Rio de Janeiro, RJ - 20921-400, Brazil, ³⁸SLAC National Accelerator Laboratory, Menlo Park, CA 94025, USA, ³⁹Ruhr University Bochum, Faculty of Physics and Astronomy, Astronomical Institute, German Centre for Cosmological Lensing, 44780 Bochum, Germany, ⁴⁰Laboratoire de physique des 2 infinis Irène Joliot-Curie, CNRS Université Paris-Saclay, Bât. 100, F-91405 Orsay Cedex, France, ⁴¹Department of Physics and Astronomy, Pevensey Building, University of Sussex, Brighton, BN1 9QH, UK, ⁴²Physics Department, Lancaster University, Lancaster, LA1 4YB, UK, ⁴³Computer Science and Mathematics Division, Oak Ridge National Laboratory, Oak Ridge, TN 37831, ⁴⁴Center for Astrophysical Surveys, National Center for Supercomputing Applications, 1205 West Clark St., Urbana, IL 61801, USA, ⁴⁵Central University of Kerala, Kasaragod, Kerala, India, ⁴⁶Berkeley Center for Cosmological Physics, Department of Physics, University of California, Berkeley, CA 94720, US, ⁴⁷Lawrence Berkeley National Laboratory, 1 Cyclotron Road, Berkeley, CA 94720, USA

Appendix A. Data

ID	Redshift	Observer Frame Time Lag (days)	JAV-ICCF Gap (days)	Peak–Median Cut	Peak Proportion	Final Quality Rating
DES J022514.39-044700.14	1.928	217 ± 50	37	gold	0.945	gold
DES J022327.85-040119.16	1.922	396 ± 33	50	gold	0.68	gold
DES J022537.03-050109.34	1.936	294 ± 17	13	gold	0.346	bronze
DES J033401.79-265054.28	1.952	604 ± 29	61	bronze	0.389	bronze
DES J025159.70-005159.89	1.988	113 ± 27	45	gold	0.822	gold
DES J032703.62-274425.27	2.031	556 ± 35	19	gold	0.39	bronze
DES J002959.21-434835.24	2.041	442 ± 18	2	gold	0.482	silver
DES J021921.81-043642.21	2.092	379 ± 29	8	gold	0.375	bronze
DES J021941.16-044100.36	2.096	413 ± 36	19	gold	0.357	bronze
DES J032829.96-274212.23	2.15	480 ± 27	34	bronze	0.355	bronze
DES J032939.97-284952.40	2.188	237 ± 31	11	gold	0.357	bronze
DES J022001.63-052216.92	2.219	599 ± 49	6	gold	0.63	gold
DES J003743.89-434715.68	2.257	527 ± 23	52	silver	0.529	silver
DES J033655.83-290218.23	2.283	499 ± 25	76	gold	0.364	bronze
DES J022410.96-050653.95	2.315	552 ± 42	3	gold	0.735	gold
DES J033843.76-294922.54	2.328	307 ± 12	3	gold	0.667	gold
DES J004056.56-431446.40	2.384	295 ± 37	5	gold	0.331	bronze
DES J025102.06-004142.78	2.425	227 ± 40	1	gold	0.578	silver
DES J022354.81-044814.94	2.452	934 ± 31	83	gold	0.51	silver
DES J024511.94-011317.50	2.462	116 ± 37	6	bronze	0.336	bronze
DES J025100.64+001707.38	2.459	409 ± 37	71	bronze	0.359	bronze
DES J032640.93-283206.80	2.492	507 ± 15	41	gold	0.484	silver
DES J003957.42-434107.92	2.5	512 ± 17	19	gold	0.384	bronze
DES J022259.87-063326.65	2.563	325 ± 23	18	gold	0.435	bronze
DES J003352.72-425452.55	2.593	386 ± 14	65	bronze	0.409	bronze
DES J022330.15-043004.09	2.677	331 ± 20	53	gold	0.349	bronze
DES J022620.86-045946.48	2.745	378 ± 21	6	gold	0.425	bronze
DES J024514.93-004101.83	2.773	260 ± 31	25	gold	0.351	bronze
DES J025105.13-001732.01	3.451	307 ± 24	2	gold	0.537	silver

Table 1. All 29 high quality lags measurements and final quality ratings. Lags are in the observer-frame.

ID	Final Quality Rating	Rest-Frame Lag (days)	Luminosity ($\lambda L_{1350\text{\AA}}$ erg s ⁻¹)	Linewidth (km s ⁻¹)	BH Mass ($10^8 M_{\odot}$)
DES J022514.39-044700.14	gold	74 ± 17	1.82×10^{46}	3610 ± 31	8.4 ± 2.7
DES J022327.85-040119.16	gold	136 ± 11	3.54×10^{45}	3808 ± 171	17.2 ± 4.3
DES J022537.03-050109.34	bronze	100 ± 6	6.95×10^{45}	4190 ± 34	15.3 ± 3.6
DES J033401.79-265054.28	bronze	205 ± 10	9.74×10^{45}	3605 ± 77	23.3 ± 5.5
DES J025159.70-005159.89	gold	38 ± 9	1.78×10^{45}	4239 ± 135	6 ± 2
DES J032703.62-274425.27	bronze	183 ± 12	1.27×10^{46}	4398 ± 43	30.9 ± 7.4
DES J002959.21-434835.24	silver	145 ± 6	6.11×10^{46}	3595 ± 11	16.4 ± 3.8
DES J021921.81-043642.21	bronze	123 ± 9	1.1×10^{46}	3519 ± 125	13.3 ± 3.3
DES J021941.16-044100.36	bronze	133 ± 12	4.69×10^{45}	4146 ± 83	20 ± 5
DES J032829.96-274212.23	bronze	152 ± 9	8.88×10^{45}	2791 ± 59	10.3 ± 2.5
DES J032939.97-284952.40	bronze	74 ± 10	7.7×10^{45}	3929 ± 138	10 ± 2.7
DES J022001.63-052216.92	gold	186 ± 15	7.54×10^{45}	3548 ± 64	20.4 ± 5
DES J003743.89-434715.68	silver	162 ± 7	1.39×10^{46}	3672 ± 60	19.1 ± 4.5
DES J033655.83-290218.23	bronze	152 ± 8	1.6×10^{46}	4228 ± 77	23.7 ± 5.6
DES J022410.96-050653.95	gold	167 ± 13	6.16×10^{45}	3647 ± 57	19.4 ± 4.7
DES J033843.76-294922.54	gold	92 ± 4	5.61×10^{45}	2781 ± 198	6.2 ± 1.6
DES J004056.56-431446.40	bronze	87 ± 11	1.61×10^{46}	3655 ± 44	10.1 ± 2.7
DES J025102.06-004142.78	silver	66 ± 12	2.27×10^{45}	3317 ± 172	6.3 ± 1.9
DES J022354.81-044814.94	silver	271 ± 9	3.82×10^{46}	4134 ± 23	40.4 ± 9.4
DES J024511.94-011317.50	bronze	34 ± 11	7.83×10^{45}	4021 ± 90	4.8 ± 1.9
DES J025100.64+001707.38	bronze	118 ± 11	7.59×10^{45}	—	—
DES J032640.93-283206.80	silver	145 ± 4	7.56×10^{45}	4328 ± 58	23.7 ± 5.5
DES J003957.42-434107.92	bronze	146 ± 5	9.86×10^{45}	3636 ± 57	16.8 ± 3.9
DES J022259.87-063326.65	bronze	91 ± 6	8.99×10^{45}	4352 ± 95	15 ± 3.6
DES J003352.72-425452.55	bronze	107 ± 4	3.44×10^{46}	3876 ± 19	14 ± 3.3
DES J022330.15-043004.09	bronze	90 ± 5	4.21×10^{45}	—	—
DES J022620.86-045946.48	bronze	101 ± 6	4.43×10^{45}	3650 ± 104	11.7 ± 2.8
DES J024514.93-004101.83	bronze	69 ± 8	5.92×10^{45}	—	—
DES J025105.13-001732.01	silver	69 ± 5	1.35×10^{46}	—	—

Table 2. All 25 successfully recovered black hole mass measurements. Four sources had successful lag measurements yet lack BH masses. This is because their CIV line suffered from major absorption features, which prevented an accurate measure of the linewidth, which we use as a proxy for the velocity dispersion used in Equation (1).